IOPscience iopscience.iop.org

Home Search Collections Journals About Contact us My IOPscience

A study of bilayer phosphorene stability under MoS_2-passivation

This content has been downloaded from IOPscience. Please scroll down to see the full text.

2017 2D Mater. 4 025091

(http://iopscience.iop.org/2053-1583/4/2/025091)

View the table of contents for this issue, or go to the journal homepage for more

Download details:

IP Address: 18.62.1.100
This content was downloaded on 27/06/2017 at 20:48

Please note that terms and conditions apply.

You may also be interested in:

Two-dimensional hexagonal semiconductors beyond grapheme
Bich Ha Nguyen and Van Hieu Nguyen

Toward high-performance two-dimensional black phosphorus electronic and optoelectronic devices
Xuefei Li, Xiong Xiong and Yanqing Wu

Synthesis, properties and applications of 2D non-graphene materials
Feng Wang, Zhenxing Wang, Qisheng Wang et al.

Enhanced stability of black phosphorus field-effect transistors with SiO2 passivation
Bensong Wan, Bingchao Yang, Yue Wang et al.

Van der Waals stacked 2D layered materials for optoelectronics
Wenjing Zhang, Qixing Wang, Yu Chen et al.

2D Materials Advances: From Large Scale Synthesis and Controlled Heterostructures to Improved Characterization Techniques, Defects and Applications
Zhong Lin, Amber McCreary, Natalie Briggs et al.

Oxygen induced strong mobility modulation in few-layer black phosphorus
Cheng Han, Zehua Hu, Alexandra Carvalho et al.

Photonics and optoelectronics of two-dimensional materials beyond graphene
Joice Sophia Ponraj, Zai-Quan Xu, Sathish Chander Dhanabalan et al.

Light–matter interaction in transition metal dichalcogenides and their heterostructures
Ursula Wurstbauer, Bastian Miller, Eric Parzinger et al.

2D Materials

RECEIVED
2 February 2017

REVISED
4 April 2017

ACCEPTED FOR PUBLICATION
20 April 2017

PUBLISHED
5 May 2017

PAPER

A study of bilayer phosphorene stability under MoS_2-passivation

Youngwoo Son[1,4], Daichi Kozawa[1,4], Albert Tianxiang Liu[1], Volodymyr B Koman[1], Qing Hua Wang[2] and Michael S Strano[1,3]

[1] Department of Chemical Engineering, Massachusetts Institute of Technology, Cambridge, MA 02139, United States of America
[2] Materials Science and Engineering, School for Engineering of Matter, Transport and Energy, Arizona State University, Tempe, AZ 85287, United States of America
[3] Author to whom any correspondence should be addressed.
[4] These authors contributed equally to this work.

E-mail: strano@mit.edu

Keywords: phosphorene, chemical stability, black phosphorus, van der Waals heterostructures

Supplementary material for this article is available online

Abstract

Despite the unique properties of black phosphorus (BP) and phosphorene, including high carrier mobility and in-plane anisotropy, their stability has been hampered by significant crystal deterioration upon exposure to oxygen and water. Herein, we investigate the chemical stability of MoS_2-passivated black phosphorus (BP) or bilayer (2L) phosphorene van der Waals (vdW) heterostructures using the field-effect transistor (FET) and phototransistor effects, measuring the persistence of conductivity and carrier mobility upon atmospheric exposure. Four thicknesses of MoS_2-passivated BP FETs were studied at 1.5 (assigned to bilayer), 5, 13, and 20 nm to elucidate the effects of the MoS_2 passivation layer on the device stability and electrical characteristics under dark and illumination (wavelength, $\lambda = 600$ nm) conditions. We find that trilayer MoS_2 passivation enhances the photoresponse of a 2L-phosphorene optoelectronic heterojunction by 78% without gate bias. When in contact with a trilayer MoS_2 layer, the photoluminescence quantum yield of the phosphorene bilayer crystal apparently decreases 29%. This can be attributed to the difference in absorption in the BP layer induced by the interference color effect generated by the presence of the thin MoS_2 layer as well as a built-in electric field that forms at the BP-MoS_2 p-n interface helps to dissociate photo-generated electron–hole pairs, thereby reducing the probability of the recombination events. The effectiveness of a trilayer MoS_2 as a vdW protection layer is tested by exposing BP-MoS_2 vdW vertical heterostructures to the ambient environment for up to 3 weeks as well as annealing at high temperature (350 °C) in an inert Ar environment. We find that the MoS_2 passivation layer reduces the dark current of bilayer phosphorene, but this effect decreases with thickness. Thus, we find that 2D MoS_2 thin passivation layers provide specific chemical stability and electro-optical enhancement for transparent, flexible BP electronic and optoelectronic devices by acting not only as an atomically thin passivation layer, but also enhancing the photoresponse.

Introduction

Motivated by the discovery of an isolated, stable monolayer graphene [1], two-dimensional (2D) layered materials have generated significant research interest for new electronic and optical devices, suggesting potential as candidate materials in future nanoelectronic applications [1]. Because they are necessarily atomically thin or of unit cell thickness, 2D layered materials may provide solutions to flexible, transparent electronics without the need for laborious and sophisticated device fabrication steps to achieve thin, high-performing channel regions required for conventional semiconducting materials.

Graphene and semiconducting transition metal dichalcogenides (TMDCs) such as MoS_2, $MoSe_2$, WS_2, and WSe_2 [2–9] have been investigated most extensively to date. These TMDCs are attractive because they can often be processed so as to demonstrate direct, permanent band gaps that graphene generally lacks. They also possess electronic and optical properties that are highly dependent upon the number of layers when in their few-layer (FL) forms due to quantum confinement [6, 10]. The band gap transitions from indirect to direct

© 2017 IOP Publishing Ltd

when in the form of a single-layered crystal, rendering semiconducting TMDCs more intriguing for many optoelectronic applications [11–13].

Recently isolated 2D crystals of black phosphorus (BP) [14–30], the most stable allotrope of phosphorus at room temperature, has generated interest and excitement in the context of 2D materials due to several unique properties [31]. Similar to graphene and TMDCs, individual layers of phosphorus are held together by van der Waals (vdW) interactions in the vertical direction. However, phosphorus atoms in each layer are bonded by sp^3 hybridization with neighboring atoms, resulting in a puckered honeycomb lattice structure [32] and in-plane anisotropy in its electronic and optical properties [25, 26, 33–36]. Potential applications include plasmonic devices [26, 34, 37, 38], phonon transport engineering, which could not have been possible with other 2D materials [39].

The hole mobility of BP devices can exceed 1000 $cm^2 V^{-1} s^{-2}$ at 300 K, but passivation is needed to prevent scattering defects from diminishing this property. Similarly, current on–off ratios in the range of 10^2–10^4 have been observed, and may be important for devices constituting high-speed logic circuits [26, 40–42]. The optical band gap of a given BP system can be engineered over a wide range to accommodate the spectrum of incident electromagnetic energy by controlling its number of layers, also providing a material advantage [24, 25, 30]. While band gaps of most of TMDCs are greater than 1 eV [43], first principles calculations showed that band gap of BP is expected to vary from ~1.5–2.0 eV in its single layer form down to around 0.3 eV when the crystal thickness is around 4 nm (~8 layers) or thicker, bridging the energy gap between graphene and TMDCs, making the material suitable for near- and mid-infrared applications such as optical telecommunications [6].

What makes this feature more intriguing is the fact that the direct band gap character is maintained regardless of its thickness—TMDCs show the direct gap character only in their monolayer form—which most of optoelectronic applications find valuable [43]. Also, whereas field-effect transistors (FETs) based on MoS_2 and WS_2 show monotonic n-type transport characteristics due to the strong Fermi-level pinning near the conduction band edge [43], recent studies have demonstrated that FL BP exhibits a noticeable p-type characteristic, thereby allowing it to be used as a p-type building block in vdW p-n heterostructures [44, 45].

Despite all of these advantages, BP has its critical drawback in that it is unstable in air, undergoing irreversible degradation upon exposure to oxygen or water [46–52], which requires a proper protection scheme to take full advantage of its superior intrinsic properties. To protect BP from the degradation, passivation of BP has been accomplished by several methods to encapsulate BP. Atomic layer deposition of aluminum oxide [47, 53–56] effectively encapsulate BP and leads to stable FET devices for 8 months [54]. Chemical passivation with molecules has been also reported. Atomic force microscopy (AFM) and optical microscopy study demonstrated that surface coordination of titanium sulfonate ligand on BP enhances chemical stability of BP in water and humid air [57]. Other molecular techniques of covalent functionalization of aryl diazonium [58] and adsorption of benzyl viologen [59] work as p-type and n-type dopant, respectively, as well as a passivation layer, demonstrated by charge-transport measurements of FETs. Even atomically thin graphene [60] and hexagonal boron nitride can protect BP from exposure to ambient air [60–63] and improved FET performance especially in electron transport channel.

However, the thickness of previously studied BP was at least thicker than 3 nm and the chemical stability of atomically thin BP to the extent of bilayer or phosphorene was not investigated, which could be more sensitive to the effect of passivation layer on optical property and optoelectronic device performance. The photoresponse of BP devices passivated with 2D semiconductor was also not measured. The van der Waals hetero-junction [18, 22, 23] can add a new functionality of BP electrical transport. For instance, MoS_2 is intrinsically electron doped and exhibit n-type behavior, while BP shows p-type behavior so that p-n junction is formed on interface between BP and MoS_2 [19, 21, 64]. The advantage of using MoS_2 as a cover layer on BP is that enhancement of photoresponse due to dissociation of photo-generated electron–hole pairs at hetero-interface can be expected.

In this work, we study the chemical stability of BP or bilayer (2L) phosphorene-MoS_2 vertical vdW heterostructure FETs subject to atmospheric air-degradation, using both the transistor characteristics and phototransistor response, and measuring the dark conductivity of BP crystals. We investigate the effectiveness of a FL MoS_2 as a vdW passivation layer under an ambient environment for an extended period of time and an elevated temperature, as well as photoluminescence (PL) at the heterojunction. When brought into contact with MoS_2, the PL intensity of bilayer (2L) phosphorene is observed to be quenched by about 29% compared to that of the BP alone. This can be attributed to the difference in absorption in the BP layer induced by the interference color effect generated by the presence of the thin MoS_2 layer (detailed discussion can be found in supporting information) (stacks.iop.org/TDM/4/025091/mmedia) as well as charge transfer due to the existence of a built-in electric field at the BP-MoS_2 junction which help dissociate photo-induced electron–hole (*e*–*h*) pairs [18, 64–66]. MoS_2-passivated FL BP crystals survived at least 3 weeks of air-exposure and 2 h of annealing at 350 K in an Ar environment, while exposed bare BP crystals are severely damaged and mostly disappeared.

We then fabricate FET devices by depositing source and drain metal electrodes on both the exposed and MoS_2-passivated regions of the same BP flake for direct comparisons. Under dark condition, hole transport of a 2L-BP channel is barely impacted by the MoS_2-

passivation layer on top while electron transport is obviously improved; the influence of the MoS_2 layer on the transport characteristic becomes less significant as the thickness of BP increases. Under illumination ($\lambda = 600$ nm), in general, higher photoconductivity is detected in the MoS_2-passivated regions than the exposed BP, with photoresponse enhancement due to the MoS_2 passivation is measured to be 75% in the 2L device when $V_g = 0$ V. These results suggest that vdW passivation using thin MoS_2 films adds another strategic route toward air-protected BP-based nanoelectronics with improved photoconductivity. Future studies of chemical stability should investigate TMDCs other than MoS_2 to fine-tune the band alignment with BP for specific target applications, which should aid in the development of air-stable high performing optoelectronic devices.

Results and discussion

Characterization of BP-MoS_2 heterojunction

BP-MoS_2 vertical heterostructures were constructed by conducting dry-transfer of thin MoS_2 films, whose shape was predefined in stripes, onto BP flakes which were micromechanically exfoliated on a 100 nm thermally grown SiO_2 on a highly doped Si wafer in a N_2-filled glove box with O_2 concentration less than 0.5 ppm (detailed schematic illustration of the process is provided in the supporting information). Large-area trilayer MoS_2 films covered by photoresist were grown by the CVD process using solid S and $MoCl_5$ as precursors on a sapphire substrate in a vacuum tube furnace [47, 60–62, 67, 68]. The thickness of the MoS_2 films was verified by Raman spectroscopy and AFM height measurements, which can be found in the supporting information. Then, standard ultraviolet lithography was utilized to define stripes on the MoS_2 film, which was followed by removal of exposed areas of MoS_2 in oxygen plasma generated by an electron cyclotron resonance (ECR) reactive plasma etch system.

The shape-defined MoS_2 films were transferred using the surface-energy-assisted method [69]. In this technique, polystyrene (PS) with a molecule weight of 280 000 g mol^{-1} was dissolved in 100 ml of toluene and this solution was spin-coated with 3500 rpm for 60 s on the shaped MoS_2 on a sapphire substrate. This composite was baked at 80 °C for 15 min. A water droplet was placed on the edge of the substrate. Delaminating MoS_2-PS film was initiated by scratching the edge of the substrate. Once the film was detached from the substrate, extra water was sucked away with a paper towel. In order to avoid water exposure to BP crystals, the peeled-off MoS_2-PS film was placed on a PDMS support and left in vacuum for 2 h before brought into the glove box, and the rest of the transfer process were conducted in the glove box to complete the whole process of heterostructure fabrication without exposure to air. PS was removed by rinsing in toluene several times. This way, BP crystals become partially covered by MoS_2 stripes, allowing for direct comparison between the exposed and MoS_2-passivated regions on the same BP flake, as schematically illustrated in figure 1(a). Throughout this work, we refer to the exposed and MoS_2-passivated BP crystals as BP-only and BP-MoS_2 regions or areas, respectively.

A fabricated 2L BP-MoS_2 heterostructure was first identified by optical contrast, and then its layer number was verified using atomic force microscope (AFM) image, profile, and Raman spectroscopy in air, as shown in figures 1(b)–(d), respectively. Before the measurements, it took within 20 min to identify the location of BP with desired thickness and within 20 min to perform take an image of AFM and Raman spectroscopy respectively. The top panel of figure 1(d) shows a representative Raman spectrum of the BP-only area taken at the location marked by the yellow dot (I) in figure 1(b) where the three signature Raman peaks of BP, attributing to the A_g^1, B_{2g}, and A_g^2 phonon modes, are prominently observed. And it is clearly observed that BP-MoS_2 region (the bottom panel, taken at the spot marked by the red dot (II) in figure 1(b)) shows corresponding Raman peaks of both BP and MoS_2 with the peak positions barely shifted from that of each homogenous crystal, corroborating successful fabrication of the heterostructure without impacting on the vibration modes of the component layers. The AFM height profile acquired along the red line marked in figure 1(b) indicates the thickness of the BP flake is ~1.5 nm which is slightly larger than the theoretical value of ~1.2 nm for a 2L BP. This has commonly been seen in measuring thickness of other 2D materials using the AFM, and it might have been worsened in the case of BP by partial oxidation and water molecules adsorbed on the crystal surface because the AFM measurements were conducted in ambient conditions after all the electrical measurements were completed [70].

The bilayer nature of the BP crystal was further confirmed by representative PL spectra in air shown in figure 1(e) taken under a green laser excitation ($\lambda = 532$ nm). To minimize the photooxidation of BP, we kept 1.9 kW cm^{-2} of incident power density, which is below the fluence that causes photooxidation ($>$10 kW cm^{-2}) [48]. A strong PL signal at around 863 nm (1.43 eV) was detected due to its direct gap character irrespective of its layer number [31]. Notably, when the BP is in contact with MoS_2, its maximum PL intensity is considerably quenched by about 29% and the peak position is blue-shifted by ~60 nm. One possible route for the quenching is reabsorption of the emitted light from BP by the MoS_2 passivation layer. However, considering the optical band gap of trilayer (3L) MoS_2 is ~1.4 eV [71] as well as its indirect gap nature, the probability of the events where the emitted photons from the 2L BP with an energy of 1.43 eV are absorbed by MoS_2 is expected to be insignificant. Another plausible mechanism for the observed quenching is the exciton dissociation by the built-in electric field formed at the BP-MoS_2 interface [13]. As illustrated in the inset in figure 1(e),

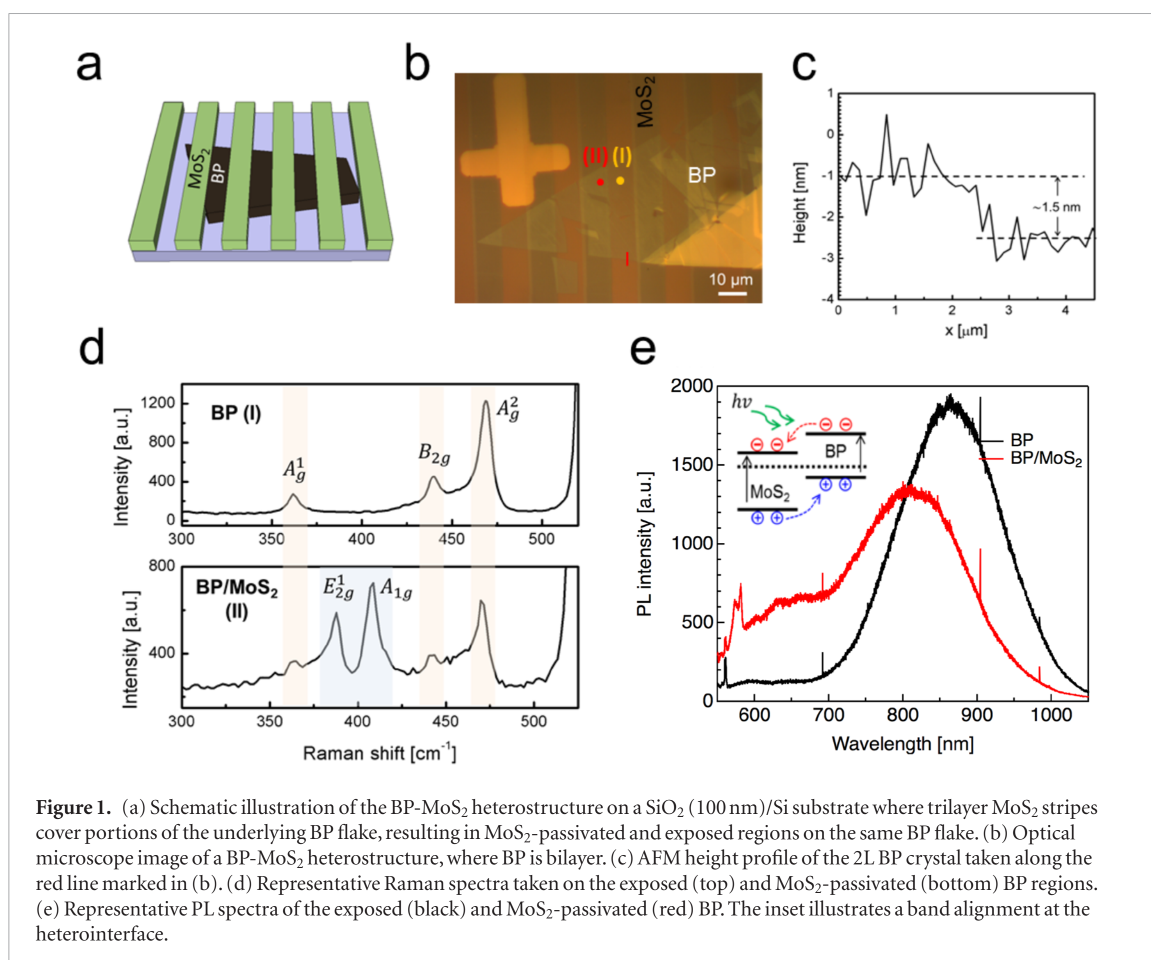

Figure 1. (a) Schematic illustration of the BP-MoS_2 heterostructure on a SiO_2 (100 nm)/Si substrate where trilayer MoS_2 stripes cover portions of the underlying BP flake, resulting in MoS_2-passivated and exposed regions on the same BP flake. (b) Optical microscope image of a BP-MoS_2 heterostructure, where BP is bilayer. (c) AFM height profile of the 2L BP crystal taken along the red line marked in (b). (d) Representative Raman spectra taken on the exposed (top) and MoS_2-passivated (bottom) BP regions. (e) Representative PL spectra of the exposed (black) and MoS_2-passivated (red) BP. The inset illustrates a band alignment at the heterointerface.

the type-II band alignment forms at the hetero-interface in which a valence band offset is larger than the counterpart of the conduction band. Because the exciton binding energy of 2L BP crystals sitting on a SiO_2 substrate is calculated to be 0.25 eV [19–21], these sizeable band offsets promote the exciton dissociation events, thereby resulting in considerably reduced recombination events. The blue shift in the PL maximum peak position upon contacting MoS_2 may be due to the reduced defect states induced by oxidation, affecting its electronic band structures.

MoS_2 as a van der Waals passivation layer

To test the effectiveness of MoS_2 thin films as a protection layer, we characterized the BP-MoS_2 heterostructures using an optical microscope and Raman spectroscopy as the samples are stored under exposure to air or an elevated temperature (350 °C). It has been reported that BP crystals quickly degrade in ambient conditions within a matter of days, with a possible mechanism involving irreversible conversion of BP into PO_x by O_2 and H_2O [29, 47, 60]. The top panel of figures 2(a) and S2, and the bottom panel of figure 2(a) show optical microscopic images of a FL BP flake which is partially covered by 3L CVD MoS_2 upon the completion of the heterostructure fabrication, after 1 and 3 weeks of exposure in air, respectively. In a week (figure S2), portions of the BP-only region have undergone severe deterioration whereas the BP-MoS_2 area remained almost intact. After 3 weeks of air-exposure, as shown in the bottom panel of figure 2(a), most of the exposed BP was etched away barely leaving traces of a BP crystal to be identified, but no noticeable change was observed in the MoS_2-passivated BP. Note that we observe no significant difference of color contrast between edge and center part of BP-MoS_2. If the color contrast exhibited a distinct difference within the width of MoS_2 stripe, the edge degradation played a major role in the crystal deterioration, which was not observed. Therefore, we believe that 10 μm width of MoS_2 stripe is enough to compare the performance of bare BP and BP-MoS_2. To further confirm this observation, Raman spectroscopy measurements were taken on both the passivated (I) and exposed (II) locations of the BP flake (figure 2(b)). In the upper panel, MoS_2-protected BP clearly shows its signature peaks—A_g^1, B_{2g}, and A_g^2 peaks—even after 3 weeks of air-exposure although the peak intensity of BP peaks decreased a little when compared to that of MoS_2, which is stable enough to withstand this level of ambient conditions over an extended period of time. Also, the spectra of the MoS_2 before and after the exposure are almost identical, in both peak shift as well as intensity, excluding a possibility of reactions at the BP-MoS_2 interface. On the other hand, the Raman spectra acquired at the exposed BP area after 3 weeks-exposure to air shows no discernable peaks associated with BP crystals, corroborating the observation under an optical microscope.

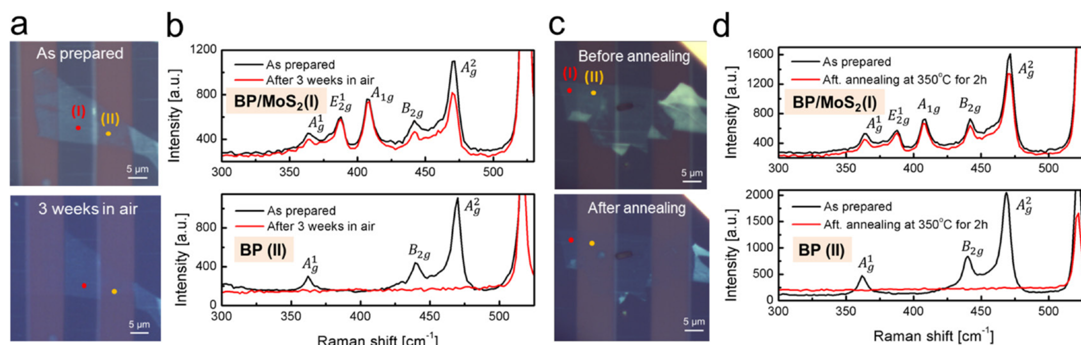

Figure 2. Stability of a few-layer BP-MoS_2 heterostructure. (a) Optical images of a BP-MoS_2 heterostacks acquired upon fabrication (top) and after 3 weeks of exposure to air (bottom). (b) Representative Raman spectra taken at exposed (bottom) and MoS_2-passivated BP (top) upon preparation and in 3 weeks in air. (c) Optical images of a BP-MoS_2 hetero-stacks acquired upon fabrication (top) and after annealing under Ar environment at 350 °C for 2 h (bottom). (d) Representative Raman spectra taken at MoS_2-passivated BP (top) and exposed (bottom) upon preparation and the annealing.

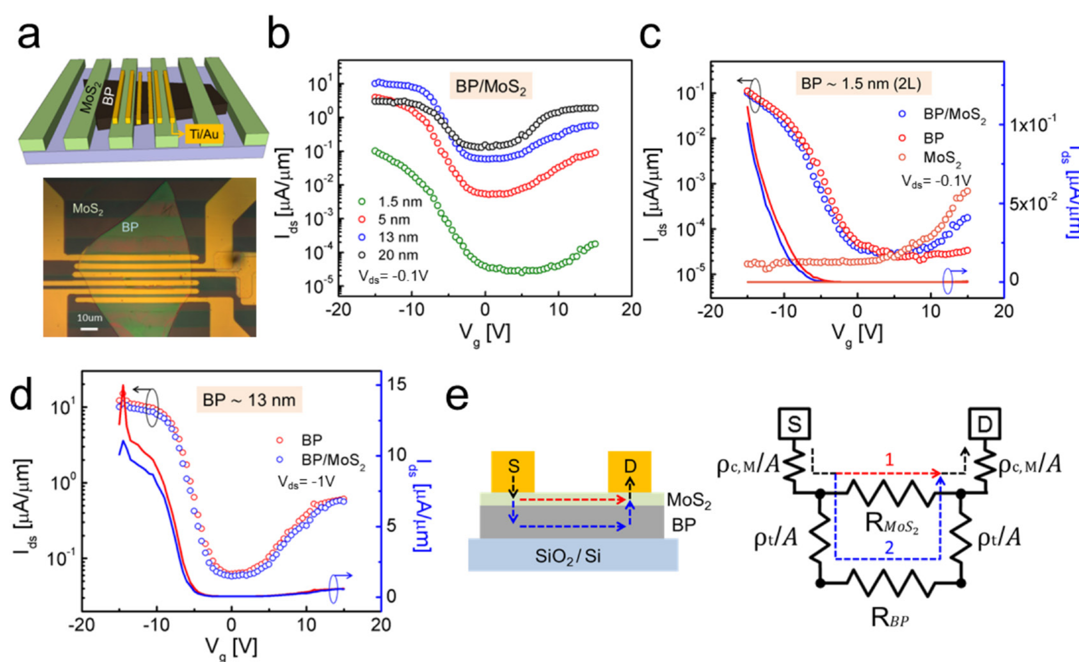

Figure 3. Transport characteristics of BP-MoS_2 heterostructures. (a) Schematic illustration of the FET devices (top) and an optical image of the 13 nm device (bottom). (b) Transfer characteristics (at $V_{ds} = -0.1$ V) of the MoS_2-passivated BP channels of varying thicknesses—1.5 (2L), 5, 13, and 20 nm. (c) Detailed transport characteristics of the 2L device where red, blue, and orange circles indicate I_{ds}–V_g traces for the BP-only, BP-MoS_2, and MoS_2-only regions, respectively. (d) Transfer characteristics of the 13 nm device where red and blue circles represent the BP-only and BP-MoS_2 regions, respectively. For (c) and (d), the left and right axes correspond to log and linear scale, respectively. (e) A simplified resistor network model that represents carrier transport pathways in the BP-MoS_2 region.

In addition, the thermal stability of a thin BP passivated by a 3L CVD MoS_2 has been tested at 350 °C under an Ar environment for 2 h, as provided in figure 2(c), where the top and bottom panels present optical images of the BP-MoS_2 heterostructure before and after the annealing, respectively. Similar to the air-stability case, the exposed BP crystal has mostly disappeared after the annealing while the MoS_2-passivated regions can still be observed by optical contrast. Again, Raman analysis was conducted at both the passivated (I) and exposed (II) locations to verify the quality of the BP crystal after the annealing (figure 2(d)). The conspicuous signature peaks of BP observed in the passivated region after the annealing confirm that the BP underneath the MoS_2 layer has survived the harsh annealing condition, with somewhat reduced peak intensity, while the exposed area has almost completely been etched away.

Transport characteristics of BP-MoS_2 heterostructure-based FETs

FET devices based on the BP-MoS_2 heterostructures were fabricated to investigate the influence of the MoS_2 passivation layer on the electrical characteristics of the underlying BP crystals. Figure 3(a) shows a schematic illustration (top) and an optical image (bottom) of the heterostructure device where the source and drain electrodes are located on both the BP-only and BP-MoS_2 regions on the same BP flake. After fabricated

inside the glove box, on top of 100 nm SiO_2 on a highly doped Si wafer which was used as a global back gate, the heterostructures were transported for further metal electrodes deposition in an N_2-filled container to minimize air-exposure. Then, the source and drain metal electrodes with a channel length of 1.5 μm were patterned on both the exposed and MoS_2-passivated areas of a target BP flake using ultraviolet photolithography, followed by the deposition of Ti (20 nm)/Au (60 nm) as the contact metal via electron beam evaporation. This way, we were able to fabricate exposed and MoS_2-passivated BP FET devices on the same BP flake, allowing for direct comparisons. In order to explore the effect of BP thickness on device performance, four different FETs out of 1.5 (2L), 5, 13 and 20 nm-thick BP flakes were fabricated with the thickness of the MoS_2 passivation layer kept constant at 3L. The AFM measurements to verify the thickness of the samples were performed in tapping mode after the electrical testing has been completed to avoid crystal degradation by air-exposure as well as possible physical damage during the imaging. The electrical measurements of the devices were carried out in an ambient environment at room temperature. More detailed fabrication and characterization methods are provided in the supporting information.

The electrical measurements were carried out using Agilent E5262A Source Measure Units for voltage sourcing and current measurements. In figure 3(b), transfer characteristics of the BP-MoS_2 channels with different BP thicknesses are plotted at constant source-drain voltage, $V_{ds} = -0.1$ V. In general, we find that the on-current increases prominently as the gate voltage (V_g) sweeps towards negative voltage which we assign to p-type transport characteristics, consistent with previous reports for BP FETs [47]. This indicates that the metal electrodes interact with the BP channel through the thin MoS_2 passivation layer and the Fermi level is then pinned closer to the valence band of the BP. Hence, the transport within the channel is largely determined by the bottom BP channels rather than the top MoS_2 layer. This behavior is more prominent in devices based on thinner BP flakes as expected while electron transport becomes important when BP thickness reaches 20 nm (black circles, figure 3(b)), showing a near ambipolar behavior. Also, there exists an obvious trend that the minimum off-current monotonically increases, whereas the on-off current ratio (I_{on}/I_{off}) decreases as BP thickness increases—about 5×10^3 and 3×10^1 for the 2L and 20 nm devices, correspondingly (which is an underestimation of the intrinsic value of the devices given the curves do not reach the saturation within the range of voltage sweep used in this work). This can be explained by the combination of a significant change in the band gap of BP with the layer number and a consequent Schottky barrier height change at the interface with the metal electrodes, discussed in more detail below. The maximum on-current, however, does not exhibit the monotonic upward trend and even decreases as the BP thickness increases from 13 to 20 nm, which could be explained by the interplay between charge screening and interlayer coupling that can be used to estimate current distribution throughout the individual layers of a 2D layered channel region [24, 25, 72–74]. The substantial interlayer resistance reduces field effect mobility in thicker BP flake [73, 75]. When the thickness of BP increases, the increased interlayer resistance prevents more current to flow the top layer far away from the bottom gate. In consequence, channel conductivity and field effect mobility consequently drops as BP becomes thicker.

The field-effect mobility of the BP-MoS_2 regions is estimated based on the method of trans-conductance [73, 76]. Specifically, the trans-conductance, g_m, is given by:

$$\mu = \frac{L}{W \times C_{ox} \times V_{ds}} \left| \left(\frac{\partial I_{ds}}{\partial V_g} \right) \right|_{V_{ds}} \quad (1)$$

where L and W correspond to the effective channel length and width between drain and source electrodes, respectively. C_{ox} is the capacitance of the gate oxide, I_{ds} is the drain-source current, V_{ds} is the drain-source voltage, and V_g is the back-gate voltage. The estimated field-effect hole mobility values (μ) are: 0.5, 15.7, 50.6, and 14.7 cm^2 V^{-1} s^{-1} for 1.5 (2L), 5, 13, and 20 nm devices, respectively. These are comparatively lower than previously reported hole mobility predictions for exposed [77] and AlO_x-encapsulated [24] BP devices, which could be due to increased scattering events from additional defect, trap and impurity states introduced at the BP-MoS_2 interface and the imperfect dry transfer of MoS_2 thin films.

More detailed results of the 2L device are provided in figure 3(c) where direct comparisons between the BP-only, BP-MoS_2, and MoS_2-only channels can be made. Firstly, the BP-only channel (red circles) exhibits an obvious p-type characteristic with a negligible level of electron transport recorded under a positively applied V_g up to 15 V. In contrast, the MoS_2-only channel (orange circles) shows an n-type behavior with no discernable hole transport, but with maximum I_{ds} of only ~7×10^{-4} μA μm which is around a hundred times lower than that of the BP-only and with an I_{on}/I_{off} of mere ~50. The much lower conductance of the MoS_2 channel than the BP channel even with one more layer available for charge carrier transport could be in part attributed to the heavier effective mass in MoS_2 and the low crystal quality of the CVD-grown MoS_2 film, which is a common trade-off for large area 2D films grown by the CVD process. In the BP-MoS_2 region (blue circles), under a negative back gate voltage, the current trace is very close to that of the BP-only channel with only a little decrease in the current level, implying that a FL-thin MoS_2 passivation layer does not add noticeable impedance and the tunneling barrier in the vertical direction is relatively insignificant in comparison to the Schottky barrier that forms in the lateral direction toward the

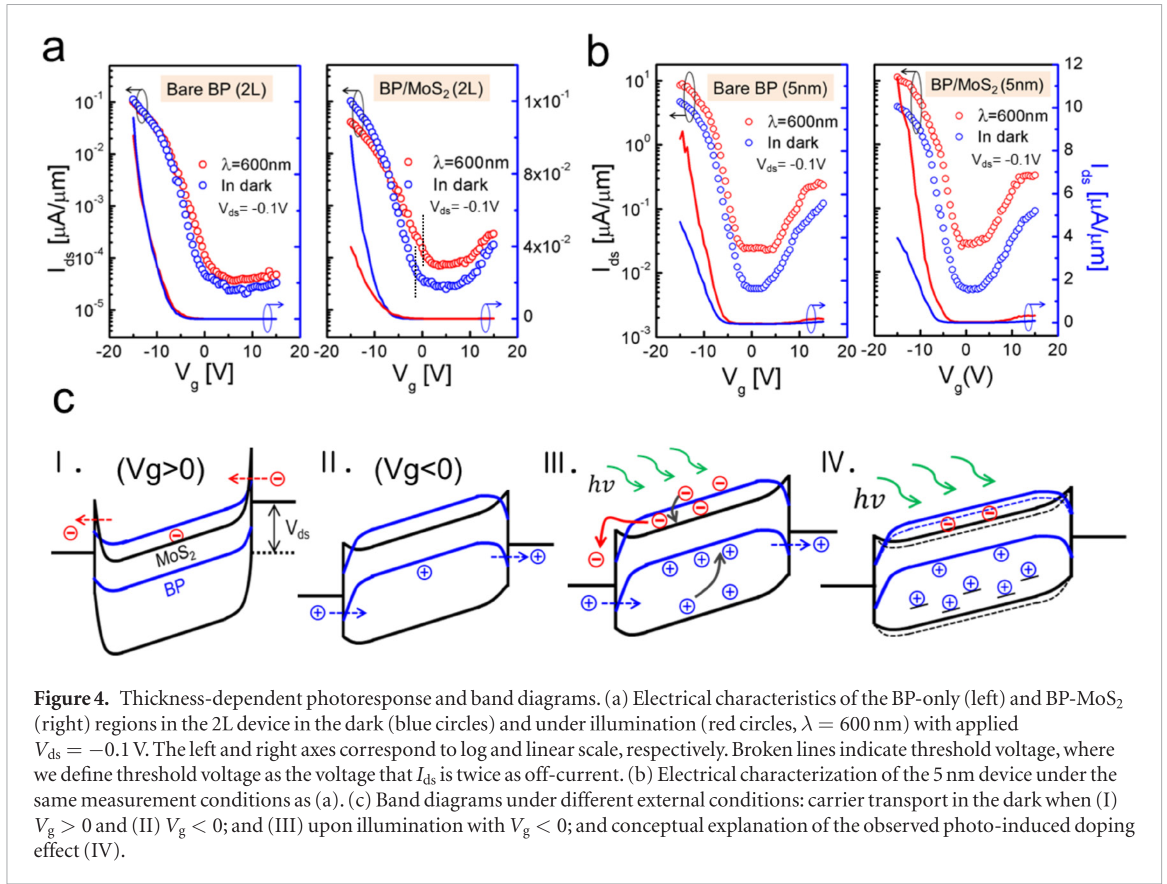

Figure 4. Thickness-dependent photoresponse and band diagrams. (a) Electrical characteristics of the BP-only (left) and BP-MoS_2 (right) regions in the 2L device in the dark (blue circles) and under illumination (red circles, $\lambda = 600$ nm) with applied $V_{ds} = -0.1$ V. The left and right axes correspond to log and linear scale, respectively. Broken lines indicate threshold voltage, where we define threshold voltage as the voltage that I_{ds} is twice as off-current. (b) Electrical characterization of the 5 nm device under the same measurement conditions as (a). (c) Band diagrams under different external conditions: carrier transport in the dark when (I) $V_g > 0$ and (II) $V_g < 0$; and (III) upon illumination with $V_g < 0$; and conceptual explanation of the observed photo-induced doping effect (IV).

channel. However, interestingly, as V_g changes its polarity and sweeps to large positive voltages, the BP-MoS_2 channel begins to show distinct electron transport although its magnitude is slightly lower than the MoS_2-only. Since the carrier transport through the BP and MoS_2 layers can be considered independent in the BP-MoS_2 region [47], the transport pathways can be simplified using a resistor network schematically illustrated in figure 3(e), where carrier injection into the BP channel encounters an additional tunneling barrier across the upper MoS_2 passivation layer. The total device conductivity can be expressed as:

$$\sigma = (2\rho_{c,M}/A + R_{ch})^{-1} \tag{2}$$

where, $R_{ch}^{-1} = R_{MoS_2}^{-1} + (2\rho_t/A + R_{BP})^{-1}$ and $\rho_{c,M}$ is the contact resistivity at the metal electrodes-MoS_2 interface, R_{ch} is the channel resistance, ρ_t is the vertical tunneling resistivity across the MoS_2 passivation layer, A is the electrodes contact area, and R_{MoS_2} and R_{BP} are the individual MoS_2 and BP channel resistances, respectively.

When negative V_g is applied, $R_{MoS_2} \gg R_{BP}$ which leads to $R_{ch} \sim (2\rho_t/A + R_{BP})$ and, consequently, $\sigma = [2\rho_{c,M} + \rho_t)/A + R_{BP}]^{-1}$. Hence, the BP channel dominates the overall carrier transport, as indicated as blue dotted arrow in figure 3(e), with the MoS_2 acting mainly as an encapsulation layer rather than a conductive channel for charge carrier transport. From the observation that almost the same I_{ds}–V_g characteristics were measured for the BP-only and BP-MoS_2 with a large negative applied V_g, it is expected that $\rho_{c,BP} \sim \rho_{c,M} + \rho_t$; but, $\rho_{c,M} + \rho_t$ becomes a bit more important as a smaller magnitude of negative V_g is applied. In the positive V_g regime, R_{MoS_2} (R_{BP}) decreases (increases) that carrier transport along the top MoS_2 channel (red dotted passage in figure 3(e)) becomes of significance. For V_g larger than ~5 V, the BP-MoS_2 shows much higher channel conductivity than the BP-only, but still lower when compared to the MoS_2-only. This may also be because of more defects, scattering sites introduced at the heterointerface as well as a lower gating efficiency due to the charge screening by the underlying BP channel.

Conceptual understanding of this observation can be aided by the gate-dependent band diagrams, schematically illustrated in figure 4(c). Under a positive V_g (I), the Schottky barrier for electron injection to the conduction band of MoS_2 becomes thin such that the conductivity of the MoS_2 channel increases, while hole injection to the valence band of BP becomes favorable when a negative V_g is applied (II), resulting in improved conductivity in the BP channel. When the thickness of BP flakes is 5 nm or more (see figures 3(d), S3(d) and S5(d), 4(a) and (b)), because a BP channel has many more layers for current passage than MoS_2, $R_{MoS_2} \gg R_{BP}$ over the whole range of V_g so that the current flow is largely determined by the BP channel, causing for BP-MoS_2 regions to show an almost identical I_{ds}–V_g curve to corresponding BP-only regions—slightly lower current values were due to the introduced tunneling resistivity from the MoS_2 passivation and defect, scattering sites added during the heterostructure fabrication process. Thus, our results suggest that thin MoS_2

films can be considered as a candidate passivation layer which in general does not deteriorate transport characteristics of BP FETs while even boosting electron transport when an ultrathin BP flake is used—2L in this study.

Enhanced photoresponse by charge separation on the interface

The transfer characteristics were also acquired under laser illumination ($\lambda = 600$ nm; 0.01 W cm^{-2}) to study the impact of the MoS_2 passivation on the photoresponse of the devices. We used a supercontinuum light source (NKT, SuperK Extreme EXR-15), which was relayed through a 600 nm bandpass filter (FWHM = 10 nm). Broad illumination was used to cover the whole device in the phototransistor measurements. Figures 4(a), (b), S4(d) and S5(e) show the I_{ds}–V_g characteristics of the devices under illumination as well as in the dark measured at $V_{ds} = -0.1$ V. Interestingly, the BP-only and BP-MoS_2 regions in the 2L BP device showed apparently different responses from each other (figure 4(a)). In the BP-only region, over most of the gate voltage sweep, a higher current was recorded upon illumination (red line) compared to that obtained in the dark (black line), which can be attributed to increased conductivity due to generated extra charge carriers upon light absorption (photoconductivity). But, this photoconductivity decreases as a V_g sweeps to a larger negative voltage so that even a slightly lower current was observed when $V_g < -12$ V. This observation becomes more prominent in the BP-MoS_2 region, as presented in the right panel of figure 4(a). Compared to the BP-only case, the degree of current enhancement is greater in the BP-MoS_2 area in the positive V_g regime as well as with a moderate negative V_g up to about −7 V, at which the photoconductivity converts into a negative response. The threshold voltage for BP-MoS_2 upon illumination and in the dark right is −1.25 V and +0.28 V, respectively, as shown in figure 4(a) right, where we define threshold voltage as the V_g that I_{ds} is twice as off-current. The shift by the illumination is −1.53 V. With no electrostatic gating ($V_g = 0$ V), photo-induced current of the BP-only region, $PR_{exp} = I_{L,exp} - I_{D,exp}$, is measured to be 7.3×10^{-3} mA W^{-1} while that of the BP-MoS_2 region was 1.3×10^{-2} mA W^{-1} and photoresponse enhancement by the MoS_2 passivation layer, ΔPR, to be 78% where the ΔPR is defined as:

$$\Delta PR(\%) = \frac{PR_{psv} - PR_{exp}}{PR_{exp}} = \frac{(I_{L,psv} - I_{D,psv}) - (I_{L,exp} - I_{D,exp})}{(I_{L,exp} - I_{D,exp})} \times 100 \quad (3)$$

where $I_{L(D),psv(exp)}$ is the current measured under illumination (in the dark) at the BP-MoS_2 (BP-only) region.

This increased photoconductivity attributed to MoS_2 suggests improved exciton dissociation efficiency by the built-in electric field at the BP-MoS_2 p-n interface—previously evidenced by the significant PL quenching—which exists throughout the whole active channel area. This provides an additional driving force for separation of photo-generated *e*–*h* pairs [78]. Some additional light absorption by the MoS_2 passivation layer may contribute to the photoconductivity by generating additional photo-induced *e*–*h* pairs, which can then be separated for electrons (holes) to be injected into the conduction (valence) band of the BP, resulting in increased channel conductivity, as illustrated in figure 4(c) (III). The observed current reduction in the BP-MoS_2 region upon illumination under a large negative V_g may originate from a photo-induced doping effect previously reported in 2D materials [19–21]. Under light illumination, a portion of the photo-generated charge carriers (holes in this case) are trapped in localized states, as sketched in figure 4(c) (IV). Then, the trapped holes partially screen a negatively applied V_g which reduces gating efficiency, leading to a horizontal shift of the I_{ds}–V_g characteristic toward a more negative gate voltage. Therefore, the photoresponse in the 2 L BP-MoS_2 can be interpreted as the combination of a noticeable increase in photoconductivity as well as the photo-induced doping effect.

Figure 4(b) shows the transfer characteristics of the 5 nm devices at the BP-only (left) and BP-MoS_2 (right) regions in the dark and with illumination under the same conditions as the 2L device. Here, higher photoconductivity was observed compared to the 2L device with the recorded PR_{exp} and ΔPR as 2.1 mA W^{-1} and 22%, respectively. That is, the absolute amount of photocurrent generation was bigger and dominates while the photoresponse enhancement due to the MoS_2 passivation layer decreased when zero gate voltage was applied ($V_g = 0$ V). In contrast to the 2L device, the photoconductive effect dominates the process and no noticeable photodoping effect was observed in both BP-only and BP-MoS_2 regions so that PR_{exp} and ΔPR of the device reached 2.5×10^2 mA W^{-1} and 71% at $V_g = -11$ V. Additional results for 13 and 20 nm devices are in the supporting information (figures S4(d) and S5(e)). At $V_g = 0$ V, as the thickness of BP increases, a continued increasing trend in PR_{exp} with 2.1×10^1 and 3.3×10^1 mA W^{-1} for the 13 and 20 nm devices, respectively; but, the enhancement by the MoS_2 passivation has decreased to mere 1% in the 20 nm device. Thus, MoS_2 passivation is shown to have a significant influence on carrier transport by introduction of channels for electron conduction as well as photoresponse in atomically thin FL BP devices. As the nature of BP crystals approaches its bulk form, the MoS_2 functions primarily as a passivation layer and its role as an electron transport/photoresponse enhancer becomes relatively insignificant.

Conclusions

In conclusion, in this work we study BP-MoS_2 vertical vdW heterostructure FETs and trilayer MoS_2 films can impart chemical stability and enhance the apparent

photoresponsivity. When exposed to open atmosphere a 3L CVD MoS_2, preserves an underlying FL BP crystal up to 3 weeks, while exposed portions of the same crystal were completely deteriorated as confirmed by Raman analysis. Moreover, the MoS_2 passivation layer provided BP with improved thermal stability such that the MoS_2-passivated regions survived 2 h of annealing at 350 °C in an Ar environment with exposed parts completely etched. When in contact with MoS_2, the PL from a 2L BP crystal is quenched by 29% compared to the bare BP crystal. This can be attributed to the difference in absorption in the BP layer induced by the interference color effect generated by the presence of the thin MoS_2 layer as well as charge transfer due to the existence of a built-in electric field at the BP-MoS_2 junction. FET devices fabricated based on BP flakes with varying thicknesses showed an interesting thickness dependent effect of MoS_2 passivation layer on electrical characteristics and photoresponse of the devices. Under the dark condition, electron transport of a 2L-thin BP channel was noticeably enhanced by the MoS_2 passivation layer apparently by the addition of electron conduction channels, while no significant change was observed in hole transport. This effect became insignificant as the thickness of BP increased so that the I_{ds}–V_g curves from MoS_2-passivated and exposed areas of the 20 nm device barely deviated from each other. Under illumination of $\lambda = 600$ nm, apparent photoconductivity was increased by 78% in the 2L device ($V_g = 0$ V) in the MoS_2-passivated region than the BP-only. In addition, a noteworthy, photo-induced doping effect was observed, becoming less significant in thicker BP devices. Hence, these results demonstrate that BP-MoS_2 vdW heterostructures provide a strategic route towards air-protected BP-based nanoelectronics with boosted photoconductivity. The introduction of different combinations of 2D materials may open up opportunities allowing for engineering of the band alignment for specific target applications.

Acknowledgment

Y Son is grateful for partial financial support from a Samsung scholarship. D Kozawa acknowledges the support of the Grant-in-Aid for JSPS Fellows (JSPS KAKENHI Grant Number 15J07423) and Encouragement of Young Scientists (B) (JSPS KAKENHI Grant Number JP16K17485) from Japan Society for the Promotion of Science. V B Koman is supported by The Swiss National Science Foundation (project no. P2ELP3_162149). M.S. Strano acknowledges a grant from the AFOSR FATE MURI, Grant No. FA9550-15-1-0514. Also, this work was supported in part by the US Army Research Laboratory and the US. Army Research Office through the Institute for US Soldier Nanotechnologies, under contract number W911NF-13-D-0001. This work was performed in part at the Harvard University Center for Nanoscale Systems (CNS), a member of the National Nanotechnology Coordinated Infrastructure Network (NNCI), which is supported by the National Science Foundation under NSF award no. 1541959.

Notes

The authors declare no competing financial interests.

References

[1] Geim A K and Novoselov K S 2007 *Nat. Mater.* **6** 183–91
[2] Liu W, Cao W, Kang J and Banerjee K 2013 *ECS Trans.* **58** 281–5
[3] Abderrahmane A, Ko P, Thu T, Ishizawa S, Takamura T and Sandhu A 2014 *Nanotechnology* **25** 365202
[4] Lopez-Sanchez O, Lembke D, Kayci M, Radenovic A and Kis A 2013 *Nat. Nanotechnol.* **8** 497–501
[5] Radisavljevic B, Whitwick M B and Kis A 2011 *ACS Nano* **5** 9934–8
[6] Wang Q H, Kalantar-Zadeh K, Kis A, Coleman J N and Strano M S 2012 *Nat. Nanotechnol.* **7** 699–712
[7] Wang H, Yu L, Lee Y H, Shi Y, Hsu A, Chin M L, Li L J, Dubey M, Kong J and Palacios T 2012 *Nano Lett.* **12** 4674–80
[8] Son Y, Li M-Y, Cheng C-C, Wei K-H, Liu P, Wang Q H, Li L-J and Strano M S 2016 *Nano Lett.* **16** 3571–7
[9] Mak K F, Lee C, Hone J, Shan J and Heinz T F 2010 *Phys. Rev. Lett.* **105** 136805
[10] Bhimanapati G R, Lin Z, Meunier V, Jung Y, Cha J, Das S, Xiao D, Son Y, Strano M S and Cooper V R 2015 *ACS Nano* **9** 11509–39
[11] Mattheiss L 1973 *Phys. Rev. Lett.* **30** 784
[12] Son Y, Wang Q H, Paulson J A, Shih C-J, Rajan A G, Tvrdy K, Kim S, Alfeeli B, Braatz R D and Strano M S 2015 *ACS Nano* **9** 2843–55
[13] Kuc A, Zibouche N and Heine T 2011 *Phys. Rev.* B **83** 245213
[14] Lee C-H, Lee G-H, Van Der Zande A M, Chen W, Li Y, Han M, Cui X, Arefe G, Nuckolls C and Heinz T F 2014 *Nat. Nanotechnol.* **9** 676–81
[15] Gao G, Gao W, Cannuccia E, Taha-Tijerina J, Balicas L, Mathkar A, Narayanan T, Liu Z, Gupta B K and Peng J 2012 *Nano Lett.* **12** 3518–25
[16] Li M-Y, Shi Y, Cheng C-C, Lu L-S, Lin Y-C, Tang H-L, Tsai M-L, Chu C-W, Wei K-H and He J-H 2015 *Science* **349** 524–8
[17] Flöry N, Jain A, Bharadwaj P, Parzefall M, Taniguchi T, Watanabe K and Novotny L 2015 *Appl. Phys. Lett.* **107** 123106
[18] Kozawa D, Carvalho A, Verzhbitskiy I, Giustiniano F, Miyauchi Y, Mouri S, Castro Neto A H, Matsuda K and Eda G 2016 *Nano Lett.* **16** 4087–93
[19] Hong T, Chamlagain B, Wang T, Chuang H-J, Zhou Z and Xu Y-Q 2015 *Nanoscale* **7** 18537–41
[20] Chen P *et al* 2015 *2D Mater.* **2** 034009
[21] Huang L, Li Y, Wei Z and Li J 2015 *Sci. Rep.* **5** 16448
[22] Roy K, Padmanabhan M, Goswami S, Sai T P, Ramalingam G, Raghavan S and Ghosh A 2013 *Nat. Nanotechnol.* **8** 826–30
[23] Jariwala D, Sangwan V K, Wu C-C, Prabhumirashi P L, Geier M L, Marks T J, Lauhon L J and Hersam M C 2013 *Proc. Natl Acad. Sci. USA* **110** 18076–80
[24] Li L, Yu Y, Ye G J, Ge Q, Ou X, Wu H, Feng D, Chen X H and Zhang Y 2014 *Nat. Nanotechnol.* **9** 372–7
[25] Liu H, Neal A T, Zhu Z, Luo Z, Xu X, Tománek D and Ye P D 2014 *ACS Nano* **8** 4033–41
[26] Xia F, Wang H and Jia Y 2014 *Nat. Commun.* **5** 4458
[27] Buscema M, Groenendijk D J, Blanter S I, Steele G A, van der Zant H S and Castellanos-Gomez A 2014 *Nano Lett.* **14** 3347–52
[28] Qiao J, Kong X, Hu Z X, Yang F and Ji W 2014 *Nat. Commun.* **5** 4475
[29] Andres C-G *et al* 2014 *2D Mater.* **1** 025001
[30] Koenig S P, Doganov R A, Schmidt H, Castro Neto A H and Özyilmaz B 2014 *Appl. Phys. Lett.* **104** 103106
[31] Castellanos-Gomez A 2015 *J. Phys. Chem. Lett.* **6** 4280–91

[32] Nishii T, Maruyama Y, Inabe T and Shirotani I 1987 *Synth. Met.* **18** 559–64
[33] Ling X, Wang H, Huang S, Xia F and Dresselhaus M S 2015 *Proc. Natl Acad. Sci. USA* **112** 4523–30
[34] Wang X, Jones A M, Seyler K L, Tran V, Jia Y, Zhao H, Wang H, Yang L, Xu X and Xia F 2015 *Nat. Nanotechnol.* **10** 517–21
[35] Yuan H *et al* 2015 *Nat. Nanotechnol.* **10** 707–13
[36] Hong T, Chamlagain B, Lin W, Chuang H J, Pan M, Zhou Z and Xu Y Q 2014 *Nanoscale* **6** 8978–83
[37] Ribeiro H B, Pimenta M A, de Matos C J, Moreira R L, Rodin A S, Zapata J D, de Souza E A and Castro Neto A H 2015 *ACS Nano* **9** 4270–6
[38] Ge S, Li C, Zhang Z, Zhang C, Zhang Y, Qiu J, Wang Q, Liu J, Jia S and Feng J 2015 *Nano Lett.* **15** 4650–6
[39] Low T, Roldán R, Wang H, Xia F, Avouris P, Moreno L M and Guinea F 2014 *Phys. Rev. Lett.* **113** 106802
[40] Luo Z, Maassen J, Deng Y, Du Y, Garrelts R P, Lundstrom M S, Ye P D and Xu X 2015 *Nat. Commun.* **6** 8572
[41] Engel M, Steiner M and Avouris P 2014 *Nano Lett.* **14** 6414–7
[42] Li P and Appelbaum I 2014 *Phys. Rev.* B **90** 115439
[43] Cai Y, Zhang G and Zhang Y-W 2014 *Sci. Rep.* **4** 6677
[44] Liu D, Guo Y, Fang L and Robertson J 2013 *Appl. Phys. Lett.* **103** 183113
[45] Gong C, Colombo L, Wallace R M and Cho K 2014 *Nano Lett.* **14** 1714–20
[46] Kistanov A A, Cai Y, Zhou K, Dmitriev S V and Zhang Y-W 2016 *2D Mater.* **4** 015010
[47] Wood J D, Wells S A, Jariwala D, Chen K S, Cho E, Sangwan V K, Liu X, Lauhon L J, Marks T J and Hersam M C 2014 *Nano Lett.* **14** 6964–70
[48] Favron A, Gaufres E, Fossard F, Phaneuf-L'Heureux A L, Tang N Y, Levesque P L, Loiseau A, Leonelli R, Francoeur S and Martel R 2015 *Nat. Mater.* **14** 826–32
[49] Joshua O I, Gary A S, Herre S J V D Z and Andres C-G 2015 *2D Mater.* **2** 011002
[50] Utt K L, Rivero P, Mehboudi M, Harriss E O, Borunda M F, Pacheco San Juan A A and Barraza-Lopez S 2015 *ACS Central Sci.* **1** 320–7
[51] Li P, Zhang D, Liu J, Chang H, Sun Y E and Yin N 2015 *ACS Appl. Mater. Interfaces* **7** 24396–402
[52] Pieter J D V, Rebekah C, Joshua O I, Matvey F, Allard J K, Holger T, Herre S J V D Z and Teun M K 2016 *2D Mater.* **3** 021002
[53] Zhu H, McDonnell S, Qin X, Azcatl A, Cheng L, Addou R, Kim J, Ye P D and Wallace R M 2015 *ACS Appl. Mater. Interfaces* **7** 13038–43
[54] Illarionov Y Y, Waltl M, Rzepa G, Kim J-S, Kim S, Dodabalapur A, Akinwande D and Grasser T 2016 *ACS Nano* **10** 9543–9
[55] Na J, Park K, Kim J T, Choi W-K and Song Y-W 2017 *Nanotechnology* **28** 085201
[56] Kim J S, Liu Y, Zhu W, Kim S, Wu D, Tao L, Dodabalapur A, Lai K and Akinwande D 2015 *Sci. Rep.* **5** 8989
[57] Zhao Y, Wang H, Huang H, Xiao Q, Xu Y, Guo Z, Xie H, Shao J, Sun Z and Han W 2016 *Angew. Chem.* **128** 5087–91
[58] Ryder C R, Wood J D, Wells S A, Yang Y, Jariwala D, Marks T J, Schatz G C and Hersam M C 2016 *Nat. Chem.* **8** 597–602
[59] Yue D, Lee D, Jang Y D, Choi M S, Nam H J, Jung D-Y and Yoo W J 2016 *Nanoscale* **8** 12773–9
[60] Doganov R A *et al* 2015 *Nat. Commun.* **6** 6647
[61] Chen X *et al* 2015 *Nat. Commun.* **6** 7315
[62] Avsar A, Vera-Marun I J, Tan J Y, Watanabe K, Taniguchi T, Castro Neto A H and Özyilmaz B 2015 *ACS Nano* **9** 4138–45
[63] Sinha S, Takabayashi Y, Shinohara H and Kitaura R 2016 *2D Mater.* **3** 035010
[64] Deng Y, Luo Z, Conrad N J, Liu H, Gong Y, Najmaei S, Ajayan P M, Lou J, Xu X and Ye P D 2014 *ACS Nano* **8** 8292–9
[65] Hong X, Kim J, Shi S F, Zhang Y, Jin C, Sun Y, Tongay S, Wu J, Zhang Y and Wang F 2014 *Nat. Nanotechnol.* **9** 682–6
[66] Yuan J, Najmaei S, Zhang Z, Zhang J, Lei S, Ajayan P M, Yakobson B I and Lou J 2015 *ACS Nano* **9** 555–63
[67] Ziletti A, Carvalho A, Campbell D K, Coker D F and Neto A C 2015 *Phys. Rev. Lett.* **114** 046801
[68] Cao Y *et al* 2015 *Nano Lett.* **15** 4914–21
[69] Yu Y, Li C, Liu Y, Su L, Zhang Y and Cao L 2013 *Sci. Rep.* **3** 1866
[70] Gurarslan A, Yu Y, Su L, Yu Y, Suarez F, Yao S, Zhu Y, Ozturk M, Zhang Y and Cao L 2014 *ACS Nano* **8** 11522–8
[71] Zhang S, Yang J, Xu R, Wang F, Li W, Ghufran M, Zhang Y-W, Yu Z, Zhang G and Qin Q 2014 *ACS Nano* **8** 9590–6
[72] Das S, Zhang W, Demarteau M, Hoffmann A, Dubey M and Roelofs A 2014 *Nano Lett.* **14** 5733–9
[73] Das S and Appenzeller J 2013 *Nano Lett.* **13** 3396–402
[74] Sui Y and Appenzeller J 2009 *Nano Lett.* **9** 2973–7
[75] Das S and Appenzeller J 2013 *Phys. Status Solidi RRL* **7** 268–73
[76] Das S, Chen H-Y, Penumatcha A V and Appenzeller J 2012 *Nano Lett.* **13** 100–5
[77] Schwierz F 2010 *Nat. Nanotechnol.* **5** 487–96
[78] Shih C-J, Wang Q H, Son Y, Jin Z, Blankschtein D and Strano M S 2014 *ACS Nano* **8** 5790–8